Supplemental Material for "A geometric defect marker predicts transport classes in directed photonic meshes"

Ahmed Alayar[1]
[1] *Independent Researcher, Kuwait*
(Dated: February 1, 2026)

S1. DIRECTED MESH ENSEMBLE AND INCOHERENT TRANSPORT MODEL

We study layered directed meshes with W parallel channels and L propagation stages. At each stage, candidate 2×2 couplers between adjacent channels are present with bulk probability p_f; a localized "knot" defect is embedded by raising the coupler probability to p_{knot} inside a compact layer–channel region. Transport is modeled in an incoherent intensity regime by nonnegative mixing,

$$x^{(\ell+1)} = T_\ell x^{(\ell)}, \qquad y = x^{(L)}, \tag{S1}$$

where T_ℓ encodes the random coupler placement and splitting for stage ℓ. The output is summarized by contrast $C = y_{\max}/\bar{y}$ and by an effective number of populated outputs $n_{\mathrm{eff}} = \exp(H)$, where H is the Shannon entropy of the normalized output intensities.

Ensembles used in the main text. *W=20 selection (Fig. 1 left).* W=20, L=50, $p_f \in \{0.105, \ldots, 0.135\}$, 20 seeds per p_f. We compare a knot-off edge reference (inject=0) against a knot-on interior operating point (inject=9). The knot occupies channels 6–14 and layers 10–18.

Fixed-injection size replicate (Fig. 1 right). W=28, L=70, $p_f \in \{0.11, 0.12, 0.13\}$, 10 seeds per p_f. Injection is fixed to channel 14 for both knot-off and knot-on instances. The knot occupies channels 9–19 and layers 14–26.

S2. CONDENSATION-DAG GEOMETRY DIAGNOSTIC (IMPLEMENTATION DETAILS)

Given the directed mesh graph, we compute strongly connected components and contract them to form the condensation DAG. On this DAG, for SCC nodes X define a one-step future-cone volume $V(X) = 1 + |N^+(X)|$ and an edge-level cone-growth proxy $\kappa(X \to Y) = V(Y) - V(X)$. As a branching observable we define $\rho(X) = \deg^+(X) - 1$.

Blocking and affine response. At scale R we block the condensation DAG into many depth-local blocks of size $\sim R$ (deterministic partitioning by depth slice and contiguous SCC ordering). For each block B we compute block averages $(\kappa_R(B), \rho_R(B))$. Across blocks we fit an affine response

$$\kappa_R \simeq a_R \rho_R + b_R, \tag{S2}$$

estimating (a_R, b_R) by least squares and by the robust Theil–Sen method. We restrict to a healthy domain of blocks (minimum block count and positive branching) to avoid degenerate fits.

Plateau selection and fixed points. We evaluate scales $R \in \{4, 5, 6, 7, 8, 9, 10\}$. To identify a scaling window we scan contiguous windows of R values from large to small and select the first window in which the robust slope a_R has small relative variation (plateau window length $k = 3$, relative tolerance 0.15). Fixed points a^*_{rob} and a^*_{LS} are defined as the median slope over the selected window for robust and LS estimators, respectively. The defect marker is $\Delta a^* = a^*_{\mathrm{rob}} - a^*_{\mathrm{LS}}$.

S3. BINNED DICTIONARY VISUALIZATION

Figure S1 shows a binned visualization of the geometry→transport dictionary, highlighting the transition band near $\Delta a^* \approx -0.25$.

S4. CLASSIFIER-QUALITY AND THRESHOLD STABILITY

To quantify predictive performance, we treat Δa^* as a one-dimensional score for the defect-enabled class (knot on). Figure S2 reports ROC curves and AUC. Figure S3 shows the distribution of Δa^* under the fixed-injection control. Figure S4 reports AUC versus p_f. Figure S5 reports balanced accuracy versus the decision threshold on Δa^*.

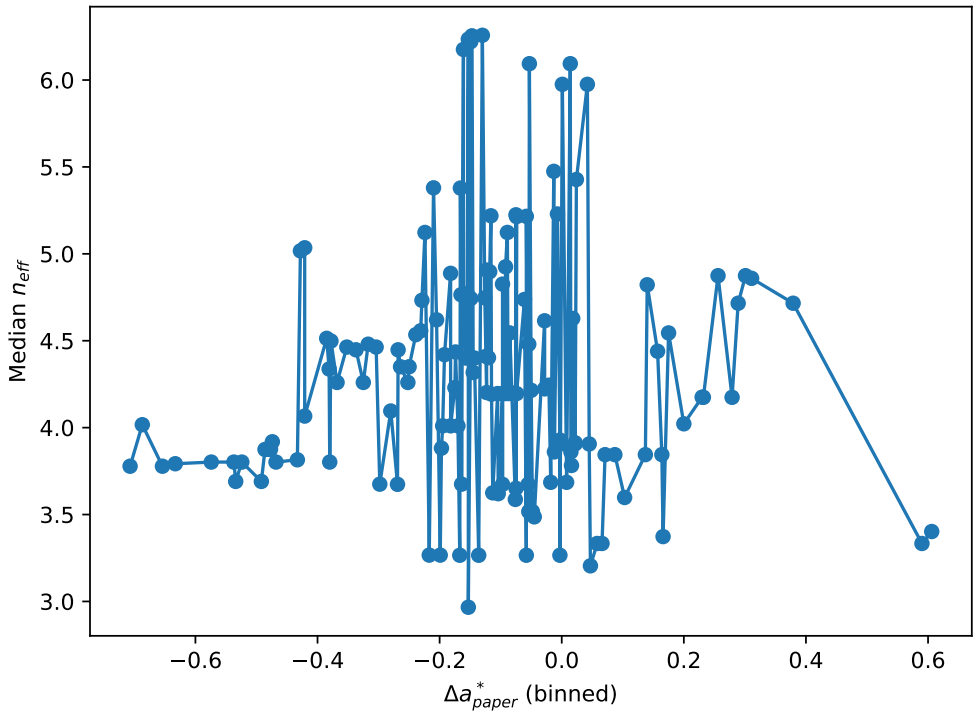

FIG. S1. **Binned geometry→transport dictionary.** Median n_{eff} within bins of Δa^* (paper convention) for the aggregated sweep.

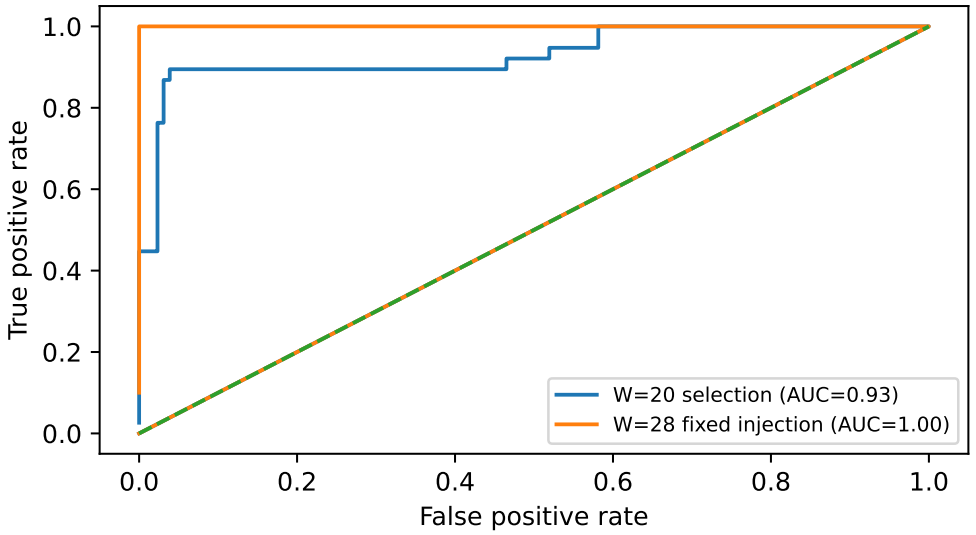

FIG. S2. **ROC curves for Δa^* as a scalar classifier.** AUC values are reported in the legend for the W=20 selection and the fixed-injection size replicate (plateau-valid subset).

S5. PLATEAU VALIDITY AND SELECTION BIAS CHECK

Because Δa^* is defined from a detected plateau window, it is undefined for "plateau-fail" instances. Figure S6 reports plateau-valid fractions for each condition. In both ensembles, excluded knot-on instances exhibit similarly high participation, indicating that plateau filtering does not artificially create the high-participation defect cluster.

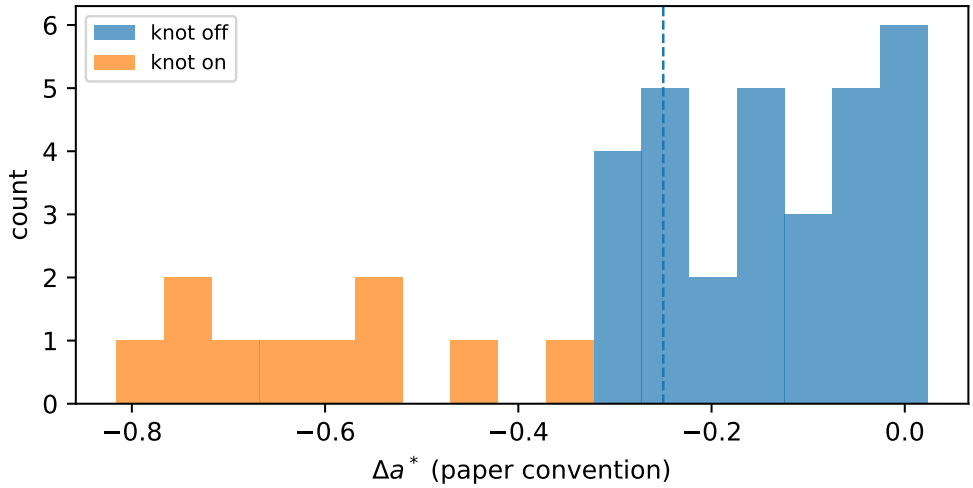

FIG. S3. Δa^* **distributions under fixed interior injection.** Overlapping histograms for knot-off and knot-on instances in the W=28 fixed-injection control.

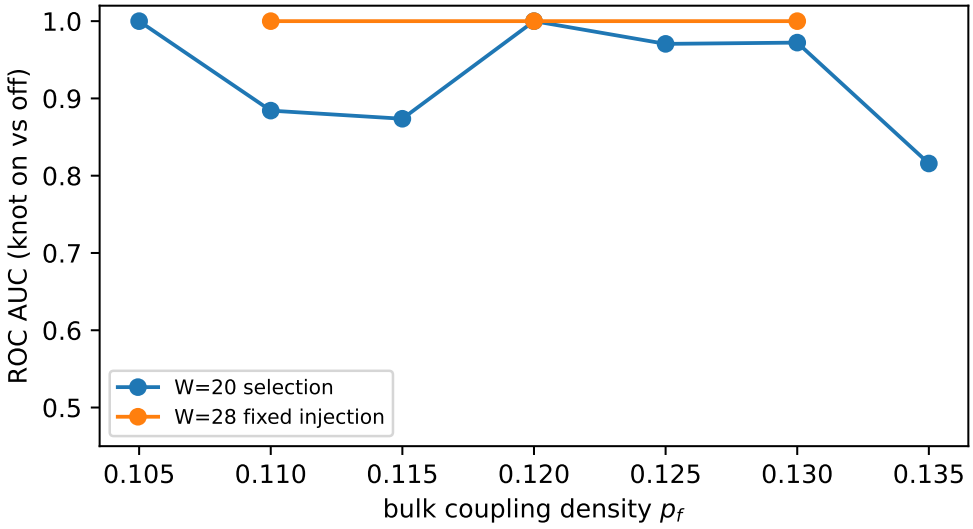

FIG. S4. **AUC versus bulk coupling density** p_f**.** Predictive performance remains high across the scanned p_f values.

S6. JITTER INVARIANCE OF DISTRIBUTIONAL OBSERVABLES

Figure S7 shows that participation and contrast are invariant across 0–50 ps jitter in our pulsed implementation.

REPRODUCIBILITY

All scripts, configurations, and processed datasets required to reproduce the figures are available at github.com/a7midi/PTPP. The figure-generation script used for the referee-facing plots is provided in the repository as `scripts/make_referee_response_figs.py`.

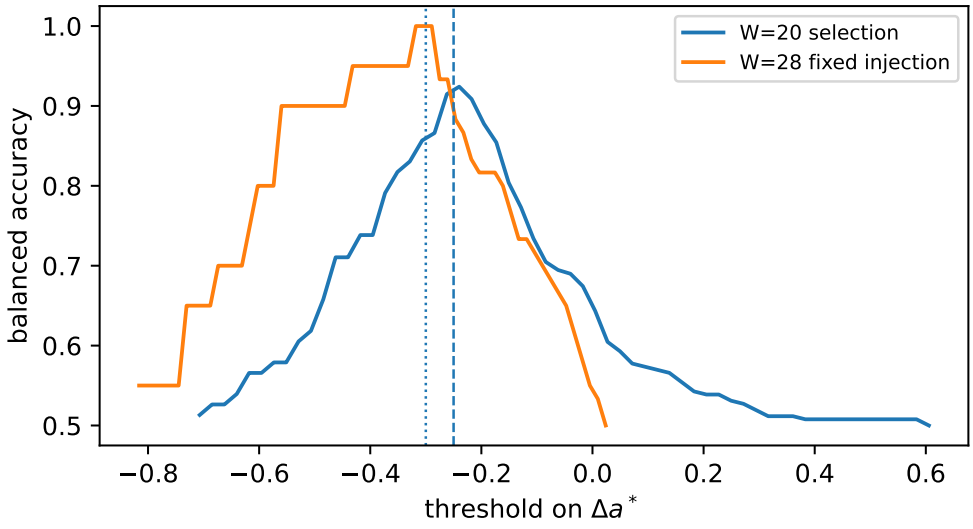

FIG. S5. **Threshold stability.** Balanced accuracy for knot-on classification as a function of a decision threshold on Δa^*. Vertical lines indicate representative operating thresholds discussed in the main text.

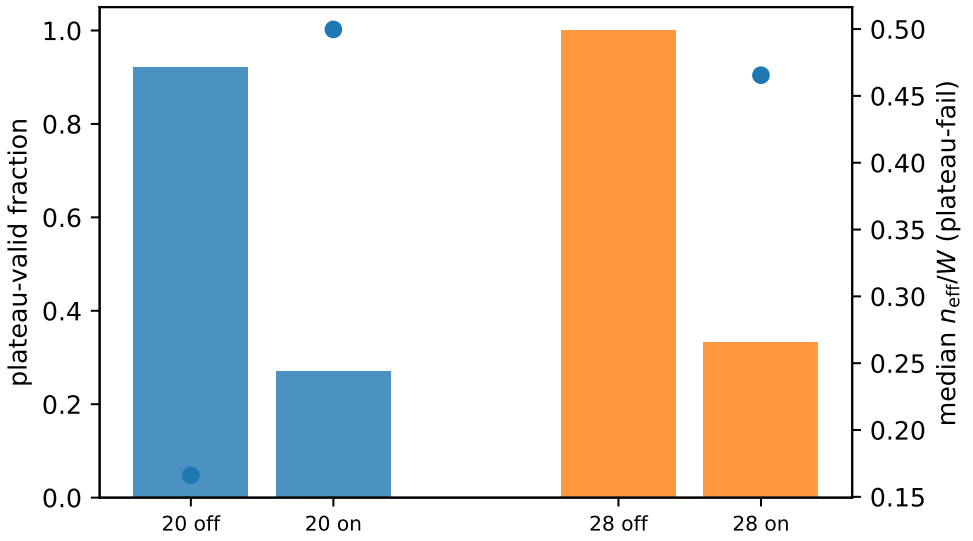

FIG. S6. **Plateau validity fractions.** Fraction of instances for which the algorithmic plateau criterion succeeds, shown for knot-off and knot-on conditions in each ensemble selection.

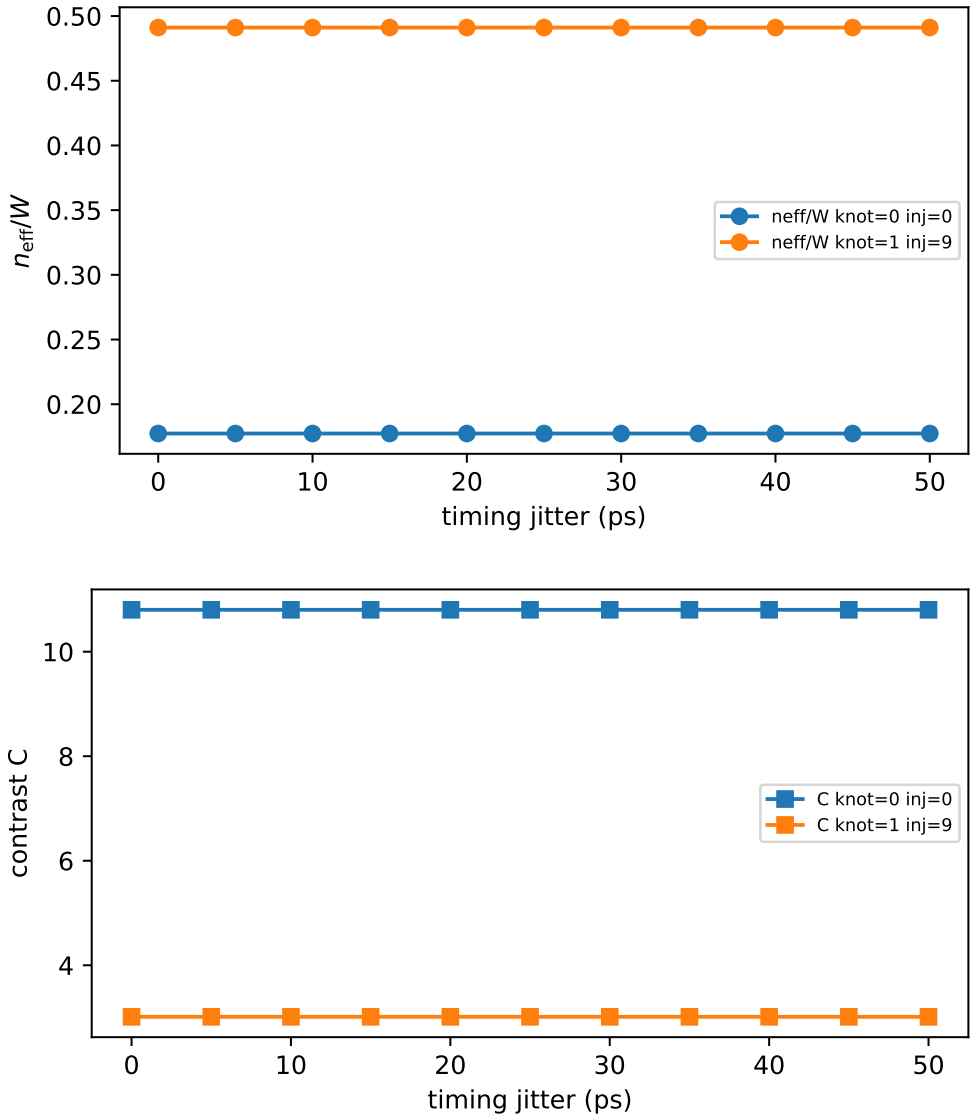

FIG. S7. **Distributional jitter invariance.** Top: mean n_{eff}/W versus jitter. Bottom: mean contrast versus jitter.